Nanoscale

PAPER

View Article Online
View Journal

Cite this: DOI: 10.1039/d5nr05162b

Corona-dependent enhanced fluorescence response of defects-induced single-walled carbon nanotubes to organophosphate

Gali Etus,[a] Srestha Basu,[b,c,d] Adi Hendler-Neumark[b] and Gili Bisker *[b,e,f,g,h,i]

Received 9th December 2025,
Accepted 9th April 2026

DOI: 10.1039/d5nr05162b

rsc.li/nanoscale

Single-walled carbon nanotubes (SWCNTs) are promising near-infrared (NIR) fluorescent nanomaterials for sensing, where their optical response is governed by surface chemistry and the surrounding corona phase. While defect engineering has been widely employed to tune SWCNT photophysics, it remains unclear how identical defects influence surface reactivity when embedded in different coronas. Addressing this gap is essential for decoupling intrinsic effects of defect introduction from extrinsic contributions of surface passivation. A deeper understanding of this interplay can inform the rational design of nanomaterials with tailored interfacial reactivity. Here, we introduce oxygen defects into (6,5) SWCNTs and demonstrate their enhanced, corona-dependent fluorescence response toward organophosphates (OPs), a model class of reactive small-molecule analytes. In sodium cholate dispersions (SWCNTs@SC), pristine nanotubes exhibit a rapid decrease in fluorescence intensity upon OP addition, whereas defect-induced SWCNTs (D-SWCNTs@SC) show amplified response. In contrast, pristine lipid–polyethylene glycol dispersions (SWCNTs@PEG) show negligible fluorescence modulation, while D-SWCNTs@PEG display a gradual fluorescence enhancement, persisting even in seawater. Fourier transform infrared and high-resolution X-ray photoelectron spectroscopy confirm direct OP-defect interactions in D-SWCNTs@SC and surface passivation in D-SWCNTs@PEG. These findings establish oxygen defects as tunable modulators of SWCNT-analyte interactions in a corona-dependent manner, offering a versatile platform for NIR fluorescence sensing.

Introduction

Single-walled carbon nanotubes (SWCNTs) are near-infrared (NIR) fluorescent nanomaterials with unique optical and electronic properties, including exceptional photostability, resistance to photobleaching, and deep tissue penetration in the NIR biological transparency window.[1–9] These features make them ideal candidates for applications in bioimaging and biosensing,[10–15] including real-time tracking of biological processes,[16,17] monitoring enzymatic activity,[18–24] and detection of hormones,[25–27] proteins,[28–30] lipids,[31] and small molecules,[32–38] among others.

The fluorescence properties of SWCNTs are strongly influenced by their surrounding corona phase, typically formed by surfactants[39,40] or polymers,[41–44] which governs the accessibility of the SWCNT surface and the fluorescence response upon interaction with target molecules.[45–51] In some cases, while the molecular coating of the SWCNTs stabilizes the dispersion, it can also restrict surface accessibility or limit the ability of pristine SWCNTs to modulate their fluorescence in response to environmental changes or as analyte binding.[52] Nevertheless, introducing covalent sp^3-hybridized defects into the SWCNT surface provides a way to overcome this limitation. Such localized defect sites alter the electronic structure of SWCNTs and can give rise to red-shifted emission features, potentially enhancing molecular accessibility and enabling tunable fluorescence modulation.[53–58] Several studies have demonstrated that sp^3-hybridized defects in SWCNTs influence their photophysical properties and enhance their interaction with the surrounding environment.[59–63] However, while the role of such defects in modulating optical behavior is

---

[a] *School of Electrical Engineering, Faculty of Engineering, Tel Aviv University, Tel Aviv 6997801, Israel*
[b] *School of Biomedical Engineering, Faculty of Engineering, Tel Aviv University, Tel Aviv 6997801, Israel*
[c] *Biophysical Sciences Group, Saha Institute of Nuclear Physics, 1/AF Bidhannagar, Kolkata 700064, India*
[d] *Chemical Sciences Division, Homi Bhabha National Institute, Mumbai 400094, India*
[e] *Center for Physics and Chemistry of Living Systems, Tel Aviv University, Tel Aviv 6997801, Israel*
[f] *Center for Nanoscience and Nanotechnology, Tel Aviv University, Tel Aviv 6997801, Israel*
[g] *Center for Light-Matter Interaction, Tel Aviv University, Tel Aviv 6997801, Israel*
[h] *Sagol School of Neuroscience, Tel Aviv University, Tel Aviv 6997801, Israel*
[i] *The Center for Computational Molecular and Materials Science, Tel Aviv University, Tel Aviv 6997801, Israel. E-mail: bisker@tauex.tau.ac.il*

investigated to a certain extent, it remains crucial to understand how these same defects influence the surface chemistry of SWCNTs when stabilized by different coronas or dispersing agents. This understanding is essential for decoupling the intrinsic effects of defect introduction from the extrinsic contributions of the surrounding chemical environment. Such insights extend beyond optical tuning, offering a broader framework for engineering defect-environment interactions in nanoscale systems relevant to catalysis, chemical sensing, molecular recognition, and bio-nano interfaces. Among the various defect chemistries, oxidative treatment with hypochlorite and ultraviolet irradiation has been shown to produce localized oxygen-containing defects characterized by their complex photophysical properties,[53,64] enabling applications such as single-particle tracking[17] and ratiometric cholesterol detection.[65]

In this study, we introduce covalent oxygen-containing defects to explore their impact on the fluorescence response of (6,5)-enriched SWCNTs dispersed in two distinct corona phases: sodium cholate (SC), a small-molecule surfactant, and lipid-polyethylene glycol (PEG), a biologically relevant dispersant. It is worth noting that the introduction of oxygen-containing sp^3 defects was deliberately chosen because it represents a well-established and widely adopted functionalization strategy in the SWCNTs literature. The NaClO/UV-mediated approach provides a reproducible and chemically well-understood route for generating oxygen-based defect sites in the SWCNTs, which have been extensively characterized in previous studies.[53] Employing this established protocol ensures that the nature of the defect sites is consistent and comparable with prior reports, thereby enabling systematic investigation of other parameters that influence defect photophysics. In the present work, the objective is to use a reliable and widely recognized defect motif as a controlled platform to probe how the surrounding corona phase modulates defect–analyte interactions. Oxygen defects are particularly suitable in this context because their chemical reactivity and associated defect-state fluorescence are sensitive to the local interfacial environment. Using such well-characterized defect sites, therefore, allows the influence of different coronas on the fluorescence response of defect-engineered SWCNTs toward a given analyte to be examined in a more generalized and interpretable manner. Consequently, the use of oxygen defects provides a chemically accessible and broadly applicable model system for understanding how corona-mediated interfacial chemistry governs the sensing behavior of defect-functionalized SWCNTs.

SC and PEG were selected as representative corona phases owing to their distinct physicochemical characteristics and modes of interaction with the SWCNT surface. SC, an ionic bile salt, stabilizes SWCNTs primarily through electrostatic and hydrophobic interactions, resulting in an adequately exposed nanotube surface.[66] In contrast, lipid-PEG provides a sterically shielded and passivated interface due to its amphiphilic phospholipid–polymer architecture.[67] These SWCNTs@SC and SWCNTs@PEG dispersions differ significantly in their surface properties and may influence the resulting accessibility to surrounding molecules as well as modulate the extent of the fluorescence response following the addition of defects.[67–69] It is worth noting that SC and DSPE-PEG represent widely used "benchmark" corona phases for dispersing SWCNTs in aqueous media. In the present study, these coronas were intentionally selected because of their well-established behavior and extensive use in the literature. Employing such standard dispersants enables the isolation of interfacial effects without the additional complexity introduced by specially designed recognition polymers. In this way, any divergence in fluorescence response can be attributed primarily to differences in the local corona environment surrounding the nanotube and its influence on defect–analyte interactions, rather than to specific chemical recognition motifs encoded within the corona itself. The use of these benchmark coronas, therefore, provides a broadly accessible model system for examining how variations in the corona phase regulate the response of defect-engineered SWCNTs to a given analyte.

To evaluate the impact of the oxygen defects and the corona phases on the fluorescence response to target analytes, we have selected organophosphate (OP) as a representative small molecule model analyte.[70] OPs are a class of phosphorus-containing compounds widely used as chemical agents found in pesticides and nerve agents, known for their toxicity, environmental persistence, and biological activity.[71] OPs were selected as representative analytes because they possess well-defined electrophilic phosphorus centers that can undergo nucleophilic substitution or addition reactions with oxygen-containing functional groups. In the context of defect-engineered SWCNTs, oxygen-based sp^3 defect sites introduce chemically reactive functionalities in the SWCNTs that can participate in such interactions. This makes OPs a suitable probe molecule to examine how defect-mediated chemical processes influence the photophysical response of SWCNTs. Additionally, the relatively small molecular size and amphiphilic nature of OP molecules enable them to access the SWCNTs surface through different corona environments, making them particularly useful for evaluating how the surrounding corona phase modulates analyte accessibility and defect reactivity. Using OP as a model analyte, therefore, allows systematic investigation of how identical defect sites embedded within different corona phases can produce divergent fluorescence responses. Consequently, OP provides a chemically relevant platform for studying the interplay between defect chemistry, analyte reactivity, and corona-mediated interfacial environments in defect-functionalized SWCNT systems. Specifically, we utilized bis[2-(methacryloyloxy)ethyl] phosphate as a chemically representative OP model. Its phosphate ester motif provides Lewis-basic oxygen atoms capable of interacting with defect sites, while its amphiphilicity ensures aqueous solubility without excessive steric hindrance, permitting differential interactions within SC and DSPE-PEG coronas. Importantly, this molecule lacks intrinsic NIR fluorescence, ensuring that any measured optical modulation originates solely from the SWCNT-analyte interaction, rather than background interference. The strong electrophilic nature of OPs and their propensity to interact with surface oxygen functionalities make them particularly suitable for probing the influence of defect-induced surface chemistry. In the context of our study, OPs thus serve as ideal analytes to evaluate how oxygen defects modulate the interfacial reactivity of SWCNTs stabilized in distinct corona environments. This choice directly aligns with our objective to discern how identical defect sites respond to external chemical stimuli under varying surface passivation conditions, thereby providing mechanistic insight into the interplay between defect chemistry and corona-dependent reactivity. By incorporating oxygen defects, we aim to amplify the optical response of SWCNTs to OPs and compare the fluorescence modulation across the SC and PEG coronas. Raman spectroscopy confirmed successful incorporation of oxygen-containing defects in both SC- and PEG-dispersed SWCNTs. Upon OP addition, oxygen defects-induced SWCNTs@SC (D-SWCNTs@SC) exhibited an immediate and more pronounced decrease in fluorescence intensity, compared to their pristine counterparts. In contrast, SWCNTs@PEG displayed no measurable response in the absence of defects, while defect-induced samples (D-SWCNTs@PEG) showed a gradual fluorescence increase that required an extended time to stabilize. Furthermore, to evaluate the robustness of this approach in complex environments, we demonstrated that D-SWCNTs@PEG retained a significant fluorescence response to OP in seawater, serving as a proof-of-concept for environmental applications. Fourier Transform Infrared (FTIR) spectroscopy analysis demonstrated that OP interacts directly with defect sites in D-SWCNTs@SC, producing distinct spectral signatures that confirm strong surface coordination. In contrast, no such interactions were evident in D-SWCNTs@PEG, where the observed fluorescence enhancement may reflect corona disruption upon defect introduction, potentially allowing surface passivation by OP.[68,72–77] Consistent with these observations, high-resolution X-ray photoelectron spectroscopy (XPS) analyses revealed the formation of new O–P and C–O–P bonds in D-SWCNTs@SC, confirming covalent interaction of OP with oxygen defect sites, whereas in D-SWCNTs@PEG, no such bonding was detected, supporting a defect passivation mechanism. These results demonstrate that both the presence of defects and the corona composition critically influence the temporal profile and direction of the fluorescence response, laying the foundation for exploring defect-corona interplay as a design principle in future SWCNT sensor platforms.

Results and discussion

To expand the applicability of introducing defects as a general strategy for modulating the optical response of single-walled carbon nanotubes (SWCNTs), we selected organophosphates (OPs) as a representative small molecule for probing SWCNT reactivity. For this purpose, oxygen defects were introduced into chirality-enriched (6,5) SWCNTs suspended by SC, a small molecule surfactant, and DSPE-PEG, a biocompatible phospholipid-polyethylene glycol.

Fluorescence response of D-SWCNTs@SC to OPs

We first assessed the spectroscopic characteristics of the (6,5) chirality-enriched single-walled carbon nanotubes (SWCNTs) dispersed in SC. UV-vis-NIR absorption analysis revealed a prominent peak at 990 nm (Fig. S1A, black curve), corresponding to the E_{11} transition. Fluorescence spectroscopy provided corroborating data of the (6,5) emission peak at 983 nm when excited at 560 nm (Fig. S1B and C, black curves), consistent with the excitation–emission map (Fig. S1D). These findings confirm the successful dispersion of the SWCNTs@SC.

To introduce oxygen defects into the prepared SWCNTs@SC, we treated the suspension with sodium hypochlorite (NaClO) and exposed it to 254 nm UV irradiation for either 5 or 15 minutes.[53] UV-vis-NIR absorption spectra of the defect-induced SWCNTs (D-SWCNTs@SC) revealed a decrease in the E_{11} peak intensity and a minor blue shift of a few nanometers for both defected samples (Fig. S1A, blue and cyan curves). The fluorescence emission profiles of the D-SWCNTs displayed a new emission peak corresponding to the E_{11}^* transition, approximately at 1110 nm for the 5 minute exposure, with $E_{11} > E_{11}^*$, and shifted to roughly 1120 nm for the 15 minute exposure, resulting in $E_{11}^* \gtrsim E_{11}$ (Fig. S1B, blue and cyan curves, respectively), with corresponding features evident in the excitation–emission maps (Fig. S1E and F). Notably, while longer UV exposure resulted in a higher E_{11}^* intensity relative to the E_{11} peak, it also led to a decrease in the overall fluorescence intensity (Fig. S1C). Therefore, the shorter UV exposure time was preferred to maintain a balance between defect formation and preserving fluorescence brightness. Finally, Raman spectroscopy on both pristine SWCNTs@SC and D-SWCNTs@SC confirmed oxygen defect incorporation in the latter, as evidenced by an increased D-band intensity at approximately 1314 cm^{-1} in the D-SWCNTs@SC (Fig. S2A). Together, these results affirm the successful introduction of defects into the surfactant-stabilized SWCNTs.

Following the spectroscopic characterization of the D-SWCNTs@SC, our investigation shifted towards evaluating their performance as optically responsive nanomaterials, specifically upon the interaction with OP. We hypothesized that the controlled introduction of oxygen defects may enhance the fluorescence response of D-SWCNTs@SC compared to pristine SWCNTs@SC. Our efforts focused on monitoring intensity modulations in the E_{11} emission peak, primarily due to its higher initial intensity and favorable signal-to-noise ratio.

Fig. 1 illustrates the fluorescence response of the pristine SWCNTs@SC and D-SWCNTs@SC suspensions with the two distinct defect levels upon exposure to OP. In the case of pristine SWCNTs@SC (Fig. 1A), OP addition led to a decrease of 55.1 ± 3.9% in E_{11} emission intensity. By contrast, the D-SWCNTs@SC prepared with 5 minute UV exposure, where the E_{11} peak remained dominant ($E_{11} > E_{11}^*$), exhibited a more substantial fluorescence decrease of 69.1 ± 1.0% (Fig. 1B). This enhanced response reflects the favorable optical modulation enabled by moderate oxygen defects introduction. However, in

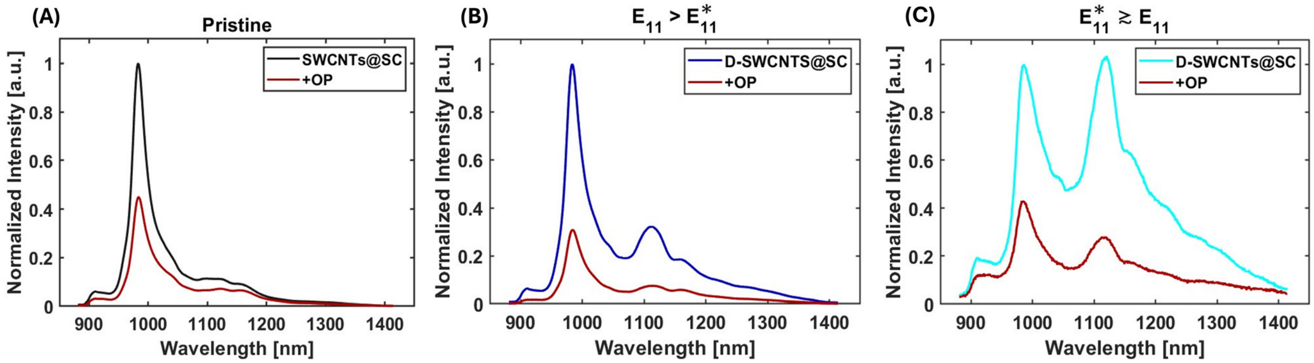

Fig. 1 Fluorescence response of pristine SWCNTs@SC and D-SWCNTs@SC suspensions to OPs. (A) Fluorescence spectrum of pristine SWCNTs@SC before (black) and after (red) the addition of OP. (B) Fluorescence spectrum of D-SWCNTs@SC, prepared with 5 minute UV exposure, before (blue) and after (red) OP addition. (C) Fluorescence spectrum of D-SWCNTs@SC, prepared with 15 minute UV exposure, before (cyan) and after (red) OP addition.

the sample generated with 15 minute UV exposure, where the E^*_{11} peak approaches or exceeds E_{11} ($E^*_{11} \gtrsim E_{11}$), the fluorescence response was attenuated, with only a 57 ± 1.2% decrease in intensity (Fig. 1C and Fig. S3). This trend suggests that excessive defect formation may weaken signal transduction efficiency. Nevertheless, the overall response of D-SWCNTs@SC for both UV exposure conditions was larger than the fluorescence response of the pristine SWCNTs@SC suspension. These results indicate that the extent of oxygen defect incorporation can be tuned to maximize the fluorescence response to OP. Notably, a preliminary selectivity test for D-SWCNTs@SC was performed using several representative inorganic phosphates and glucose phosphate, showing no measurable fluorescence response under the same conditions (Fig. S4).

The enhanced sensitivity toward OPs observed in the D-SWCNTs@SC following 5 minute UV exposure in the presence of NaClO (Fig. 1B) can likely be attributed to the critical role of defects in modifying the SWCNT fluorescence response properties.[53,78] Specifically, oxygen defects introduce localized electronic states and alter the band structure of SWCNTs, possibly creating new, more reactive adsorption sites for analytes like OPs, leading to a more pronounced fluorescence modulation.[55] This highlights that introducing defects is a powerful strategy for tuning and optimizing SWCNTs@SC fluorescence response to various analytes.

Real-time fluorescence tracking of the D-SWCNTs@SC suspension with 5 minute UV exposure, $E_{11} > E^*_{11}$, was performed under continuous acquisition with 4 second exposure intervals, with either OP or water as a control, added after approximately 40 seconds of baseline monitoring. Following OP addition, a rapid and stable decrease in the E_{11} fluorescence intensity was observed, stabilizing within roughly 5 minutes (Fig. 2A). In contrast, a control experiment with water resulted in a stable fluorescence signal with minimal fluctuations, as expected, confirming that the observed decrease upon OP exposure was indeed induced by the analyte. The full fluorescence spectra at the different time points under these continuous real-time measurement conditions are presented in Fig. S5. Raman Spectroscopy was also performed on the D-SWCNTs@SC, showing that the Raman spectrum remains largely unchanged following OP addition (Fig. S2B).

To calibrate the fluorescence response, we measured the normalized fluorescence response of D-SWCNTs@SC, calculated as $(I_0 - I)/I_0$, where I_0 and I are the initial and final fluorescence intensity, respectively, as a function of OP concentration. Indeed, D-SWCNTs@SC showed a concentration-dependent response with a typical sigmoidal trend (Fig. 2B). The data were fitted using the Hill equation,[79] $\beta \cdot \left(\frac{x^n}{{K_\mathrm{d}}^n + x^n}\right)$, where K_d is the dissociation constant, n is the Hill coefficient, β is the amplitude of the response, and x is the analyte concentration. The fit parameters were $K_\mathrm{d} = 0.81 \pm 0.11$ mM, $n = 2.3 \pm 0.6$, and $\beta = 0.75 \pm 0.04$, where the limit of detection (LOD) was calculated to be 0.070 ± 0.010 mM. These results demonstrate that oxygen defects give rise to a sensitive, rapid, and stable fluorescence response of SWCNTs to OP.

Fluorescence response of D-SWCNTs@PEG to OPs

Following the successful application of oxygen defects to enhance the fluorescence response of SWCNTs@SC towards OP, we set out to broaden the scope of this approach to an alternative dispersion involving a biologically compatible SWCNT corona of lipid-PEG, namely, 1,2-distearoyl-*sn-glycero*-3-phosphoethanolamine-*N*-[carboxy(polyethylene glycol)-2000] DSPE-PEG. To form the suspension, the SC corona of SWCNTs@SC was replaced with DSPE-PEG *via* dialysis. UV-vis-NIR absorption spectroscopy confirmed successful exchange, as evidenced by the characteristic red-shift in the E_{11} absorption peak from 989 nm to 995 nm (Fig. S6). The concentration of the resulting SWCNTs@PEG was then adjusted to match that of the SC-based system, ensuring a consistent comparison across conditions.

Next, oxygen defects were introduced to the SWCNTs@PEG sample using the same protocol with NaClO and UV exposure

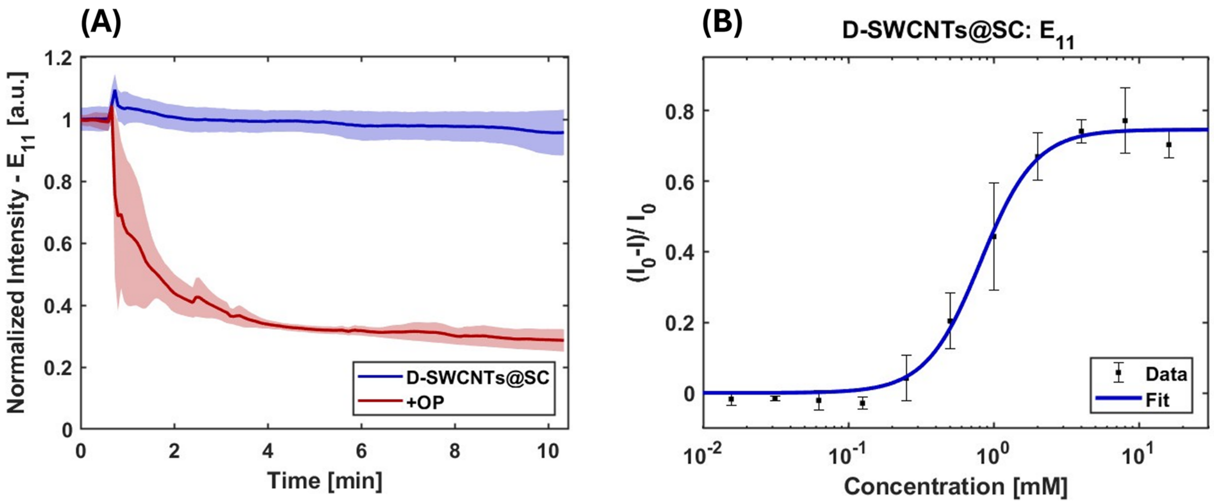

Fig. 2 Time-dependent fluorescence response and calibration of D-SWCNTs@SC. (A) Real-time fluorescence of D-SWCNTs@SC ($E_{11} > E_{11}^*$) upon water addition (control, blue) and OP addition (red). Shaded areas represent the standard deviation from three independent measurements. (B) Calibration curve of normalized fluorescence response $(I_0 - I)/I_0$ *versus* OP concentration, fitted using a Hill model. Here, I_0 represents the E_{11} fluorescence peak intensity prior to OP addition, while I corresponds to the E_{11} intensity following OP addition. These results demonstrate concentration-dependent sensing of OP using the E_{11} peak under low defect density.

for 5 minutes. Raman spectroscopy confirmed defect formation, as evidenced by a notable increase in the D-band intensity for the D-SWCNTs@PEG samples (Fig. S7A). These results are consistent with our earlier observations for SC-dispersed SWCNTs (Fig. S2A).

Following the fluorescence modulation experiments with D-SWCNTs@SC, we investigated the behavior of D-SWCNTs@PEG under similar conditions. Unlike the D-SWCNTs@SC system, where the fluorescence signal remained stable in the absence of OP, the fluorescence of D-SWCNTs@PEG gradually decreased over time, even without OP exposure. As shown in Fig. 3A, this decrease did not stabilize within 10 minutes of continuous measurement, indicating slower equilibration of the PEG corona dispersion compared to the SC system. Additionally, upon adding OP, the fluorescence intensity of D-SWCNTs@PEG exhibited a sharp decrease, followed by a slower, gradual increase, which also did not stabilize within the short measurement time window. Raman spectra of the

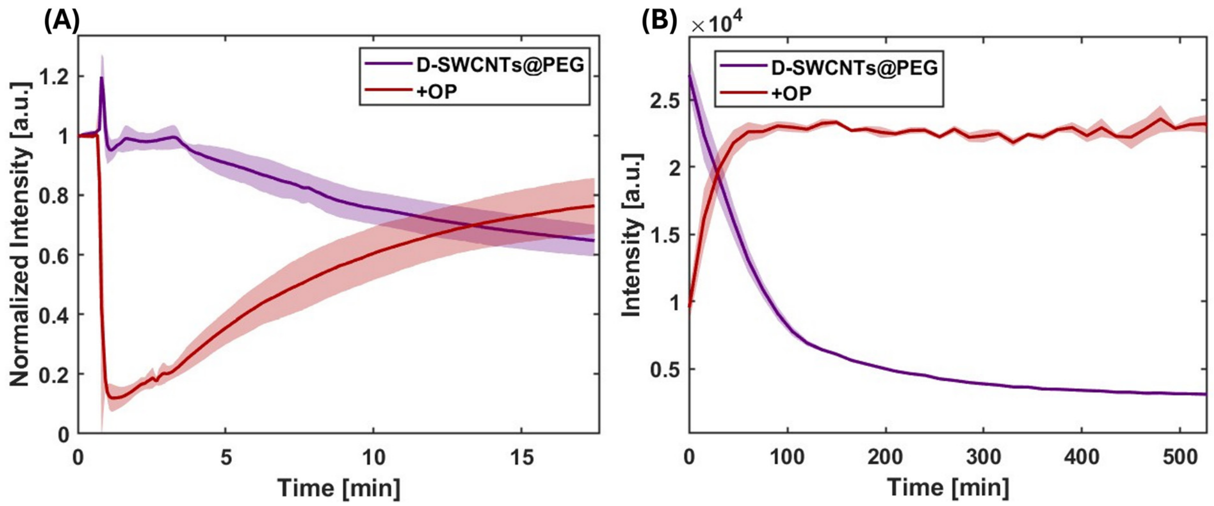

Fig. 3 Time-dependent fluorescence response of D-SWCNTs@PEG. (A) Short-term continuous real-time measurement with 4 second exposure intervals; OP (red) or water (purple) was added approximately 40 seconds after the start of acquisition. (B) Long-term fluorescence monitoring using a sequential multi-well scanning protocol with measurements taken every 15 minutes. For this measurement, the first data point was acquired approximately 5 minutes after the addition of OP (red) or water (purple) to the wells. In both short- and long-term measurements, the addition of OP (red) is compared with the control (purple), illustrating the fluorescence response behavior of D-SWCNTs@PEG under different temporal measurement regimes.

D-SWCNTs@PEG suspension remained largely unchanged before and after OP addition (Fig. S7B), as in the D-SWCNTs@SC case.

Given this time-dependent behavior, we conducted extended time-course measurements, recording fluorescence every 15 minutes for a total of 9 h (Fig. 3B). The consistency between the short- and long-term measurement protocols is evident when comparing the trends of fluorescence intensity. Specifically, the increasing and decreasing trends of the OP-treated sample intensity and the control intensity, respectively, at the 5 minute mark of the near-continuous single-well monitoring (Fig. 3A) align with the corresponding trends recorded at the start of the sequential multi-well scanning (Fig. 3B). Given that the multi-well protocol includes a ~5 minute preparation delay before the first acquisition, the long-term experiment effectively captures the subsequent evolution of the same kinetic processes observed at short times. Under these conditions, both the control and OP-containing samples continued to follow their respective decreasing and increasing trends observed in the short-term measurements, eventually reaching stable values after approximately 90–100 min (see Fig. S8 for the full spectral evolution over time). These observations reflect the dynamic nature of the corona phase, which undergoes structural reorganization following the UV/NaClO oxidative treatment. While the SC surfactant corona achieves rapid stabilization post-treatment, the DSPE-PEG interface exhibits a significantly slower equilibration process. This extended baseline evolution in the PEG system highlights the different time scales of corona reorganization, which we account for by using time-matched controls to isolate the OP-dependent response from the intrinsic stabilization of the dispersion. Crucially, after the stabilization of the fluorescence signal, the intensity from the OP-containing samples was significantly higher than that of the control, a different behavior compared to the D-SWCNTs@SC system in which OPs resulted in an intensity decrease. This behavior highlights the different fluorescence stability and interaction dynamics of defect-engineered SWCNTs in PEG compared to SC dispersions.

To highlight the effect of oxygen defects in SWCNTs@PEG on the fluorescence response toward OP, we compared the behavior of D-SWCNTs@PEG with that of their pristine SWCNTs@PEG counterparts. As shown in Fig. 4A, D-SWCNTs@PEG exhibited a clear and significant increase in fluorescence intensity 90 minutes after the addition of OP compared to the control, consistent with the time-dependent measurements (Fig. 3B). In sharp contrast, pristine SWCNTs@PEG subjected to the same conditions showed only a minimal change in fluorescence intensity upon OP addition compared to the control (Fig. 4B). These findings clearly demonstrate that oxygen defects are essential for SWCNTs@PEG to exhibit a measurable fluorescence response to OP, underscoring the essential role of defects in enabling the modulation of SWCNT fluorescence.

To further assess the applicability of the oxygen defect incorporation approach under realistic conditions, we evaluated the fluorescence response of D-SWCNTs@PEG in seawater, representing a complex matrix relevant to environmental monitoring. In this experimental workflow, the D-SWCNTs@PEG suspension was first prepared and allowed to equilibrate after defect incorporation for 2.5 hours. Seawater and OP (with seawater alone as a control) were then added, and the fluorescence response was monitored. This setup mimics practical deployment conditions in which the nanomaterials are preconditioned before use, and analyte exposure occurs only upon sample introduction.

When seawater and OP were introduced into D-SWCNTs@PEG dispersion, a clear fluorescence enhancement was observed, with the emission intensity more than doubling relative to the control (Fig. 5). Although the observed fluorescence response to OP in seawater was reduced in magnitude compared to that observed under clean laboratory con-

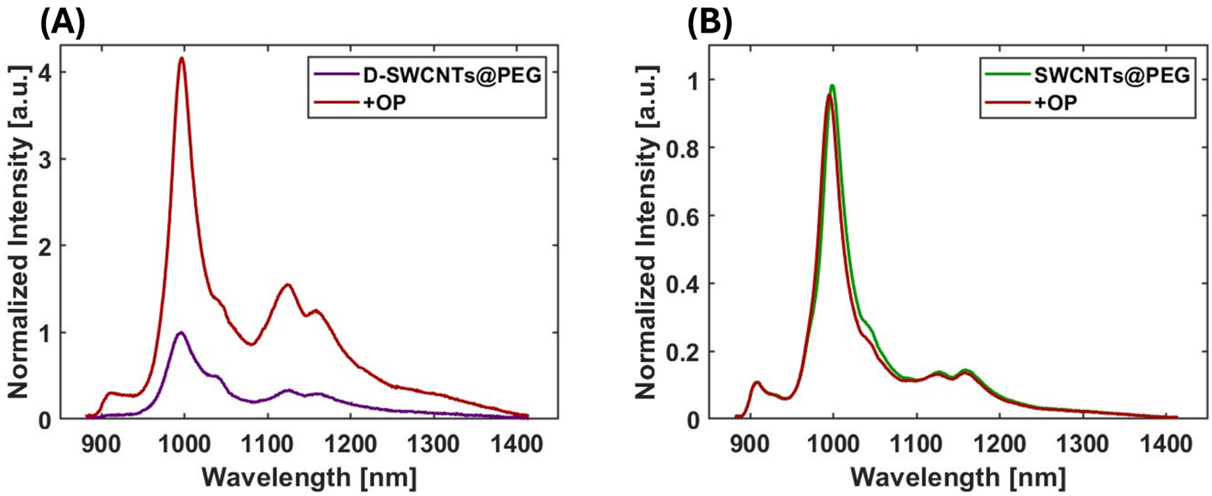

Fig. 4 Fluorescence response of pristine SWCNTs@PEG and D-SWCNTs@PEG toward OP. (A) Fluorescence intensity of D-SWCNTs@PEG 90 min after adding water (control, purple) or OP (red). (B) Fluorescence intensity of pristine SWCNTs@PEG 90 min after adding water (control, green) or OP (red). All spectra are normalized to the fluorescence intensity of the respective control sample at the 90 minute time point.

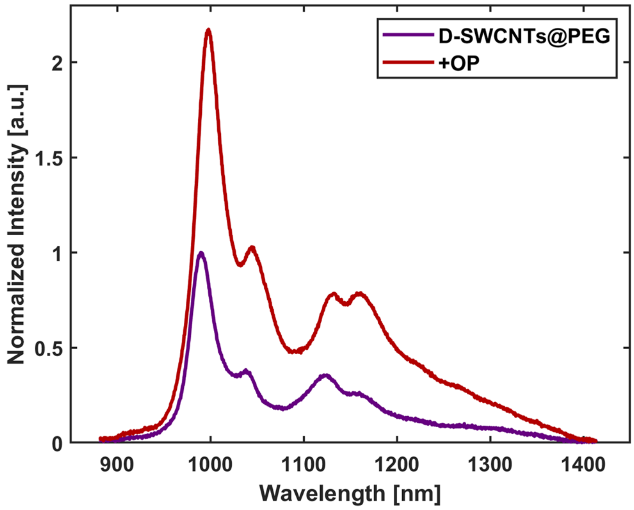

Fig. 5 Fluorescence response of equilibrated D-SWCNTs@PEG. The D-SWCNTs@PEG suspension was pre-equilibrated for 2.5 hours in water, followed by the addition of OP with seawater (red) or seawater as a control (purple).

ditions (Fig. 4A), these results demonstrate the feasibility of using D-SWCNTs@PEG as optically-responsive nanomaterials to OP in real-world samples such as seawater, serving as a promising first step toward environmental applications.

It is important to note that prior studies from our laboratory have demonstrated that oxygen defect sites in (6,5) SWCNTs suspended within a given corona environment can exhibit distinct fluorescence responses toward different neurotransmitters.[68] In those systems, the variation in response arises primarily from differences in the chemical identity of the analytes interacting with the same defect motif within an identical interfacial environment. In contrast, the present study examines how identical oxygen defect sites respond to the same analyte when the nanotubes are stabilized with different coronas. By keeping the analyte and defect chemistry constant while varying the surrounding corona phase, the current work isolates the role of the interfacial environment in regulating defect–analyte interactions. The results demonstrate that the same defect sites can produce markedly different fluorescence responses depending on the corona that surrounds the nanotube, highlighting how corona-mediated interfacial chemistry can modulate the accessibility and reactivity of defect sites toward a given analyte. This provides insight into how corona engineering can be used to tune the sensing behavior of defect-functionalized SWCNT platforms.

Mechanistic insights into the interaction of OP with defect-induced SWCNTs stabilized by different coronas

To gain mechanistic insight into the interaction of OP with D-SWCNTs@SC and D-SWCNTs@PEG compared to their pristine counterparts, we performed FTIR measurements (Fig. S9A). Upon addition of OP to D-SWCNTs@SC, the characteristic band at 1516 cm^{-1} shifted to 1552 cm^{-1} (Fig. S9B). The 1516 cm^{-1} peak is generally associated with symmetric C=C skeletal stretching in SWCNTs or aromatic ring vibrations.[80] Its shift to 1552 cm^{-1}, suggests either π–π interactions between the conjugated SWCNT framework and the methacrylate moiety of OP or modification of the local electronic environment upon binding.[81] This observation points toward a direct and stronger interaction between the OP molecule and the SWCNT surface in the presence of defects. Additionally, new peaks emerged at 1035 and 1053 cm^{-1} in the D-SWCNTs@SC added with OP (Fig. S9B). These spectral features, typically attributed to P–O–C symmetric stretching, C–O stretching, or P–O–P bridging,[82] were not observed in OP alone (Fig. S9B) or in pristine SWCNTs@SC before and after OP addition (Fig. S10). Further control experiments were conducted in which the FTIR spectra of SC (the corona) were acquired before and after treatment with OP. Notably, the aforementioned peaks were not observed in the FTIR spectra of SC either before or after exposure to OP (Fig. S11). Instead, the FTIR spectrum of SC after treatment was characterized by the additive spectral features of SC and OP. These observations suggested that the FTIR signatures detected in the presence of D-SWCNTs@SC and OP were specific to the interaction between OP and the defect sites. To rule out the possibility of SC oxidation during treatment with UV and NaClO, FTIR spectra of SC were recorded before and after exposure to these conditions. Notably, the spectral features remained unchanged (Fig. S12), indicating that the SC corona remained stable and did not undergo detectable oxidative modification upon treatment with UV and NaClO. Their exclusive appearance in the defect-containing sample suggests either conformational rearrangements of OP upon adsorption or the formation of new vibrational modes through specific interactions, such as coordination between phosphorous and defect sites on SWCNTs. Taken together, these FTIR signatures highlight that defect sites are indispensable for driving the observed interactions between D-SWCNTs@SC and OP.

In contrast, when OP was introduced to D-SWCNTs@PEG, the spectra predominantly displayed the characteristic peaks of OP, with no discernible changes in either SWCNTs@PEG or D-SWCNTs@PEG (Fig. S13). The FTIR spectra of DSPE-PEG before and after treatment with OP were also acquired. Similar to the case of SC treated with OP, only the additive spectral features of DSPE-PEG and OP were observed (Fig. S14), suggesting that no significant chemical interaction occurred between the DSPE-PEG corona and OP. FTIR spectra of DSPE-PEG were also recorded before and after treatment with NaClO and UV. Similar to the observations for SC, the spectral features of DSPE-PEG remained unchanged following treatment (Fig. S15), indicating that the corona remained chemically stable and resistant to oxidative conditions. Had OP undergone a direct reaction in this system, corresponding alterations in its spectral features would have been expected. These results suggest that OP interacts directly with defect sites in D-SWCNTs@SC but does not engage in a similar reaction with defects in D-SWCNTs@PEG. If the interactions were analogous, one would expect comparable fluorescence responses. Instead, D-SWCNTs@SC exhibited fluorescence intensity decrease, whereas D-SWCNTs@PEG showed fluorescence enhancement. A plausible explanation is that in D-SWCNTs@PEG, the introduction of defects perturbs the corona structure, thereby exposing the SWCNT surface to externally added molecules. This facilitates direct passivation of the SWCNT surface by OP, consistent with our earlier observations in the case of dopamine,[68] and is in line with previous reports where fluorescence enhancement in various nanoscale particles has been attributed to surface passivation.[72–77] Such passivation effectively removes trap states, leading to enhanced fluorescence. In contrast, for defect-free SWCNTs@PEG, the tightly packed corona prevents OP from accessing the surface, accounting for the absence of any fluorescence modulation.

To further substantiate our hypothesis, we carried out high-resolution X-ray photoelectron spectroscopic (XPS) analyses of the C 1s, O 1s, and P 2p core levels for the relevant samples. For defect-free SWCNTs@SC, the C 1s spectrum exhibited characteristic peaks corresponding to sp^2-hybridized carbon (C═C), C–O, and C═O species (Fig. S16A).[64] The O 1s spectrum revealed a dominant contribution from C–O–C functionalities (Fig. S16B).[83] Upon addition of OP, while the C 1s spectral features remained unchanged (Fig. S16C), new peaks emerged in the O 1s region corresponding to P═O and P–O bonds (Fig. S16D).[84] The accompanying P 2p spectrum confirmed the presence of phosphorus solely in the form of P–O derived from OP (Fig. S16E),[84] indicating surface adsorption

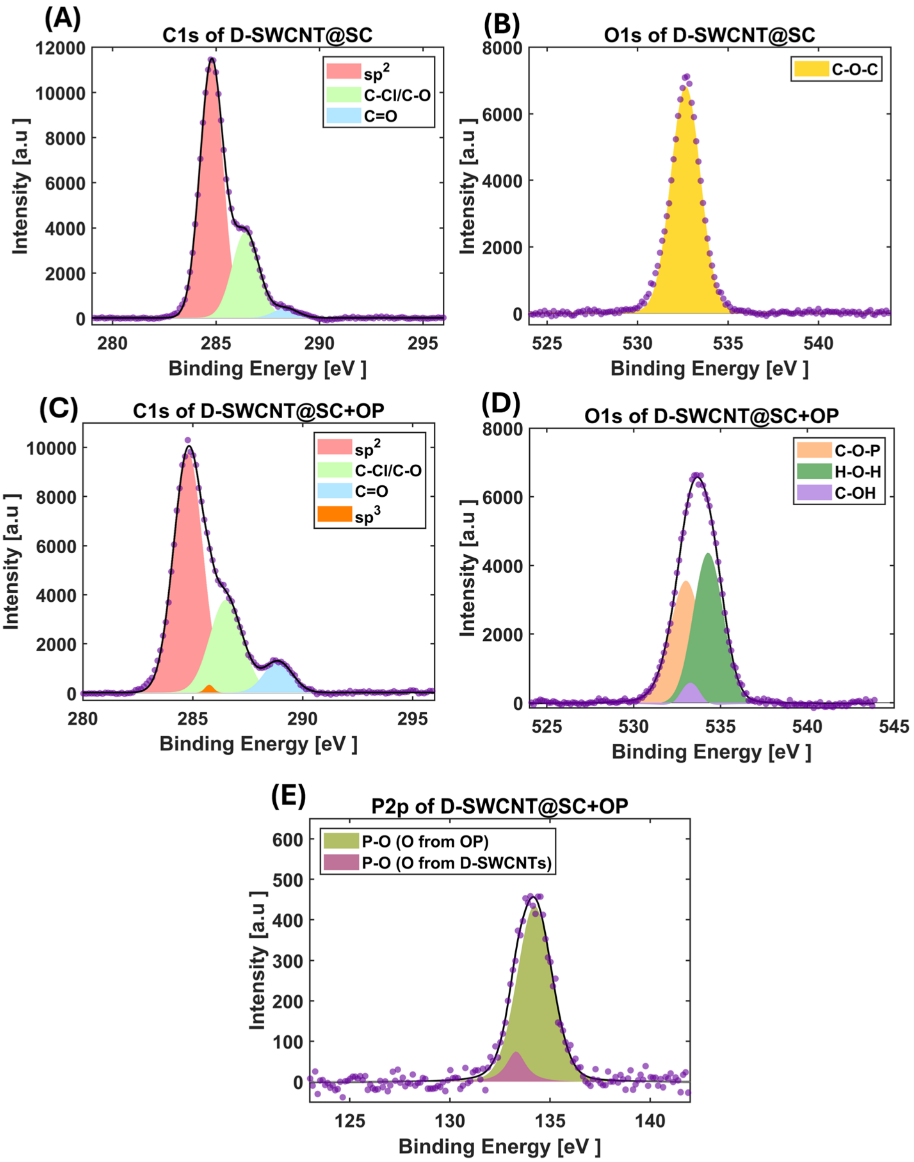

Fig. 6 High-resolution XPS spectra of D-SWCNTs@SC (A) of C 1s and (B) O 1s, before the addition of OP. High-resolution XPS spectra of D-SWCNTs@SC (C) of C 1s and (D) O 1s, after the addition of OP. (E) High-resolution XPS spectra of P 2p of D-SWCNTs@SC after the addition of OP. The colored areas represent individual deconvoluted peaks, the black line shows the cumulative fit for multiple peaks, and the purple dots correspond to the experimental data.

without any covalent interaction with the SWCNT backbone. In contrast, D-SWCNTs@SC displayed significant spectral evolution upon OP addition. In the C 1s region, we observed the characteristic peaks assigned to sp^2 carbon, C–O, and C=O for D-SWCNTs@SC (Fig. 6A),[64] and the O 1s spectrum of untreated D-SWCNTs@SC featured a peak due to C–O–C (Fig. 6B).[83] However, the OP-treated D-SWCNTs@SC revealed additional peaks attributable to sp^3 carbon in the C 1s spectrum, suggesting perturbation of the conjugated π-network and partial transformation of sp^2 to sp^3 carbon atoms (Fig. 6C),[64] and in the O 1s spectrum, new peaks attributed to C–O–P,[85] C–OH,[85] and H–O–H species,[86] clearly evidenced the formation of new O–P linkages (Fig. 6D). High-resolution P 2p analysis of OP-treated D-SWCNTs@SC further resolved two distinct P–O environments:[87] one arising from the intrinsic P–O bonds of OP, and another corresponding to newly formed P–O bonds involving oxygen defect sites on the nanotubes (Fig. 6E). These results collectively confirm the covalent bond formation between OP and oxygen defects on D-SWCNTs@SC, rationalizing the observed quenching of fluorescence in this sample upon OP addition.

For defect-free SWCNTs@PEG, the XPS spectra remained largely unaltered after OP addition. The C 1s and O 1s spectra preserved their original features, with the sole new peaks corresponding to P–O and P=O from OP adsorption, as confirmed by the P 2p spectrum (Fig. S17).[84] This indicates the

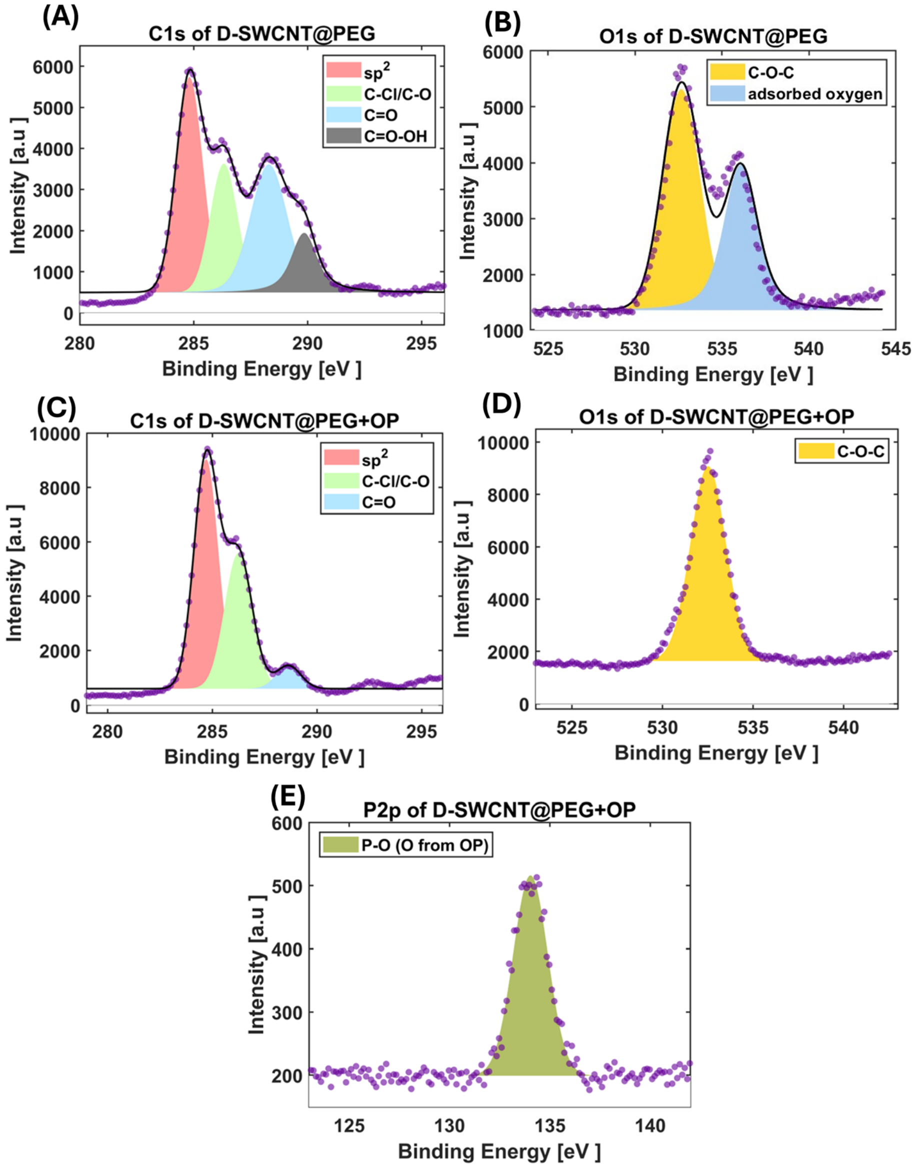

Fig. 7 High-resolution XPS spectra of D-SWCNTs@PEG (A) of C 1s and (B) O 1s, before the addition of OP. High-resolution XPS spectra of D-SWCNTs@PEG (C) of C 1s and (D) O 1s, after the addition of OP. (E) High-resolution XPS spectra of P 2p of D-SWCNTs@PEG after the addition of OP. The colored areas represent individual deconvoluted peaks, the black line shows the cumulative fit for multiple peaks, and the purple dots correspond to the experimental data.

absence of any direct chemical bonding between OP and SWCNTs@PEG. However, D-SWCNTs@PEG exhibited an additional C 1s peak assignable to C=O–OH and a corresponding O 1s peak due to adsorbed molecular oxygen, both indicative of oxygenated defect states (Fig. 7A and B).[64] Interestingly, these peaks disappeared after OP addition, implying defect passivation (Fig. 7C and D). This surface passivation effect, well known to eliminate nonradiative trap states,[76] accounts for the fluorescence enhancement observed in D-SWCNTs@PEG. Unlike in the D-SWCNTs@SC–OP system, no new P–O bonding features were detected in the P 2p spectrum (Fig. 7E), reinforcing that fluorescence enhancement in D-SWCNTs@PEG stems from defect-state passivation rather than direct chemical interaction.

Collectively, these XPS results corroborate the FTIR findings: the fluorescence quenching in D-SWCNTs@SC arises from direct OP-defect bonding, whereas fluorescence enhancement in D-SWCNTs@PEG originates from defect passivation without covalent bond formation. Taken together, the FTIR and XPS results point to two distinct interaction pathways governed by the corona environment. In the case of D-SWCNTs@SC, the appearance of new P–O-related vibrational features and additional sp^3 carbon contributions in the XPS spectra indicates covalent interaction between OP and the oxygen defect sites in the SWCNTs. Such covalent modification perturbs the local electronic structure of the nanotube, introducing additional nonradiative pathways that manifest as fluorescence quenching. In contrast, for D-SWCNTs@PEG, the absence of new P–O bonding signatures combined with the disappearance of defect-associated oxygenated features suggests passivation of defect states rather than direct covalent reaction. This passivation reduces defect-related trap states and is consistent with the observed fluorescence enhancement. These observations highlight how the corona phase can regulate the chemical reactivity of identical defect sites, ultimately dictating the direction of fluorescence modulation.

Conclusions

This study demonstrates a strategy for tuning the fluorescence response and kinetics of SWCNTs dispersed in SC and DSPE-PEG toward the model analyte, OP, by introducing oxygen defects *via* controlled UV/NaClO treatment. In SC-dispersed systems, D-SWCNTs@SC exhibited a rapid fluorescence intensity decrease upon OP addition, stabilizing within minutes. This decrease in intensity was significantly enhanced compared to their pristine SWCNTs@SC counterparts, demonstrating the role of defect incorporation in amplifying analyte-induced optical modulation. Furthermore, we demonstrated that the extent of fluorescence modulation can be tuned by varying the UV exposure time. D-SWCNTs@SC treated with 5 minute UV irradiation showed a more pronounced response, while a longer 15 minute exposure reduced the overall signal transduction efficiency, yet still produced a larger response than the pristine SWCNTs@SC suspension. These findings highlight the tunable nature of oxygen defects and the importance of optimizing the defect incorporation protocol to achieve maximal fluorescence sensitivity.

Conversely, in the PEG-dispersed systems, D-SWCNTs@PEG showed slower equilibration, but ultimately provided a stronger fluorescence response with an opposite trend, namely, an increase in fluorescence upon OP exposure. Notably, pristine SWCNTs@PEG exhibited negligible fluorescence change under identical conditions, underscoring the necessity of defect introduction to enable the observed response. These contrasting trends in the SC and PEG systems highlight the influence of the corona phase composition on the fluorescence modulation trend and kinetics, where the distinct behavior likely arises from differences in corona structure.[88,89] Importantly, we validated the platform's robustness in complex aqueous environments by demonstrating a measurable fluorescence increase of D-SWCNTs@PEG in seawater following OP addition.

FTIR and XPS analyses revealed that OPs interact directly with defect sites in D-SWCNTs@SC, forming O–P and C–O–P bonds, while in D-SWCNTs@PEG, OP-induced passivation perturbs the corona, resulting in fluorescence enhancement without new bond formation. The slower kinetics observed in PEG dispersions are consistent with diffusion-limited surface passivation, whereas SC dispersions undergo rapid, defect-mediated chemical interactions. These findings demonstrate that identical defect sites, when incorporated into SWCNTs suspended with different coronas, can elicit distinct responses to the same analyte.

While this work focused on OP as a model analyte, the mechanistic insights gained here, along with the modularity of defect introduction,[90] support broader application to other reactive target species and complex environments. Together, this approach provides a basis for developing defect-engineered SWCNT-based platforms with tunable interfacial chemistry for fluorescence modulation across chemically diverse environments.

Experimental section

SWCNT suspension with SC

10 mL of (6,5)-enriched CoMoCAT SWCNTs stock solution (2 mg mL^{-1} in 0.1 M NaCl) was mixed with 10 mL of 4% sodium cholate (Sigma Aldrich). The mixture was first bath sonicated for 10 minutes at 100% amplitude and at 80 Hz frequency. Subsequently, tip sonication was performed using a 6 mm probe at 12 W, in two 30 minute cycles to achieve a SWCNTs dispersion. Ultracentrifugation was carried out at 41 300 rpm for 4 hours to isolate well-dispersed SWCNTs from aggregates. Absorption spectra were recorded over the range of 200–1400 nm using a UV-vis-NIR spectrophotometer (Shimadzu UV-3600 Plus). Based on the absorbance at 632 nm and an extinction coefficient of 0.036 L mg^{-1} cm^{-1},[52] the SC-SWCNT concentration was calculated to be 189.7 mg L^{-1}.

Introducing oxygen defects in SC-SWCNTs

To induce oxygen defects in SC-SWCNTs, 20 μL of the stock suspension (189.7 mg L^{-1}) was diluted with 480 μL of ultrapure water. Then, 500 μL of 0.11% NaClO solution was added to the diluted sample, yielding a total volume of 1 mL. The mixture was transferred into a quartz cuvette and placed under a 254 nm UV lamp. The sample was irradiated for 5 minutes to initiate controlled oxidation, under continuous stirring at room temperature.

SWCNT suspension with DSPE-PEG

To exchange SC on the surface of SWCNTs with DSPE-PEG,1,2-distearoyl-*sn-glycero*-3-phosphoethanolamine-*N*-{carboxy(polyethylene glycol)-2000}, a dialysis was performed. First, a DSPE-PEG aqueous solution at a concentration of 5 mg mL^{-1} was prepared and sonicated thoroughly to ensure complete dissolution. Then, SC-SWCNTs were added to this solution at a concentration of 40 mg L^{-1}, resulting in a final DSPE-PEG concentration of 2 mg L^{-1}. The mixture was dialyzed against water for six days in a 1 kDa molecular weight cutoff (MWCO) dialysis tube, with the water being replaced daily. This process aimed to fully remove SC from the nanotube surfaces, thereby allowing DSPE-PEG to adsorb effectively onto the SWCNTs.

Oxygen defects in DSPE-PEG SWCNTs

Following dialysis, UV-vis-NIR absorption measurements revealed a DSPE-PEG SWCNTs concentration of 31.12 mg L^{-1}. To ensure consistency with the SC-SWCNTs protocol, the volume of the DSPE-PEG SWCNTs dispersion was adjusted to 120 μL and diluted with 360 μL of ultrapure water, maintaining the same final SWCNT concentration, prior to defect introduction. All other treatment parameters, including oxidant concentration and irradiation conditions, were kept identical to those used in the SC-SWCNTs oxidation procedure.

Near-infrared fluorescence

Fluorescence emission spectra were measured from samples placed in a 96-well plate, positioned on the stage of an inverted microscope (Olympus IX73). A 560 nm super-continuum white-light laser (NKT-photonics, Super-K Extreme) served as the excitation source. The emitted fluorescence was spectrally separated using a Spectra Pro HRS-300 spectrograph (Princeton Instruments), configured with a 500 μm slit-width and a grating of density 150 g mm^{-1}. Detection was performed with a 1D InGaAs array (PylonIR, Teledyne Princeton Instruments) operating with a 4 second exposure. To generate excitation–emission maps, excitation wavelengths were sequentially tuned from 450 to 800 nm in 2 nm increments, using the same laser.

Fluorescence response of D-SWCNTs to OP

A total of 147 μL of freshly prepared D-SWCNTs was combined with 3 μL of OP, bis[2-(methacryloyloxy)ethyl] phosphate (Sigma-Aldrich 496758) dissolved in water in a 96-well plate, yielding a final OP concentration of 8 mM. Fluorescence spectra were collected for each mixture, with background subtraction performed using water blanks. Each peak was fitted to a Lorentzian function, and the maximum of the fitted curve was taken as the fluorescence intensity maximum. To account for differences in absolute fluorescence intensity, the values were normalized to the initial intensity. During the measurements, laser power ranged between 15 mW and 17 mW.

Calibration measurements were performed in the same manner, using 11 different OP concentrations ranging from 0.015625 mM to 16 mM.

To assess selectivity, measurements were conducted with different analytes while keeping the total analyte concentration in the solution constant at 8 mM.

Time-dependent measurements

Fluorescence kinetics were evaluated using two distinct methods to capture both immediate and long-term dynamics. Short-term monitoring was conducted on individual samples, one at a time, within a single well of a 96-well plate to achieve near-continuous acquisition. A baseline was established for 40 seconds, after which OP or water (control) was added manually without interrupting the 4 second exposure intervals, capturing the immediate kinetic response. All fluorescence time-trace measurements were repeated in triplicate. In contrast, long-term monitoring was conducted for several samples across multiple conditions prepared in different wells of a 96-well plate. Due to the time required for analyte addition to multiple wells and for the initialization of the sequential scanning sequence, the first data point for each well was acquired approximately 5 minutes after analyte addition, whereas subsequent measurements were recorded every 15 minutes for 9 hours.

Fluorescence measurements with seawater

Samples of seawater were collected from the shore of the Mediterranean Sea in sterile 50 mL test tubes. The D-SWCNTs@PEG was first equilibrated in water for approximately 2.5 hours. Then, 10 μL of seawater at room temperature, along with OP (dissolved in water) at a final concentration of 8 mM, were added to the nanotube suspension. In the control experiment, only seawater was added to maintain the same total volume of the samples. Fluorescence spectra were acquired after an additional 15 minutes, with excitation at 560 nm.

Raman spectroscopy

Raman spectra were measured using a LabRAM Soleil (Horiba, France) set-up. The spectrometer was first calibrated using a silicon standard at 520 cm^{-1}. Liquid samples were then measured using the MACRO liquid attachment with a 10 × 10 mm^2 cell holder. A 532 nm laser source with a laser power of 109 mW was used during measurements. The Spectra were acquired in the 1000 cm^{-1} to 2000 cm^{-1} range with a 1800 gr per mm grating and a confocal hole of 150 μm. Measurements were repeated 3 times for each sample.

Fourier transform infrared spectroscopy (FTIR)

Fourier-transform infrared (FTIR) spectra were acquired in Attenuated Total Reflectance (ATR) mode using a PerkinElmer Spectrum Two spectrometer. Samples were prepared by dropcasting onto glass slides and drying overnight prior to analysis.

X-ray photoelectron spectroscopy (XPS)

XPS measurements were carried out using an automated ultra-high vacuum (UHV) XPS system (PHI 5000 VersaProbe II, FEI Inc.). The spectra were calibrated using the C 1s peak at 284.8 eV as the reference binding energy. High-resolution scans were acquired with an energy step size of 0.125 eV. The measurements were conducted after fluorescence stabilization, 30 min for SC suspension and 2 h for DSPE-PEG suspension. For analysis, the samples were drop-cast onto clean glass substrates and dried overnight under ambient conditions prior to measurement.

Statistical analysis

All fluorescence experiments were conducted in triplicate, and the spectra shown represents the average of three independent measurements. Each sample's fluorescence spectra were normalized to its initial fluorescence intensity. The fluorescence responses, illustrated in bar diagrams, represent averages of three independent measurements, with accompanying error bars denoting the standard deviation. In the case of D-SWCNTs, triplicate measurements correspond to independent aliquots drawn from the same defect-functionalized SWCNT dispersion and measured in separate wells. When larger volumes were required, multiple defect-functionalization batches were prepared under identical conditions and pooled prior to measurement to ensure representative ensemble behavior. Data visualization and analysis were performed using MATLAB.

Conflicts of interest

There are no conflicts to declare.

Data availability

The data are available upon reasonable request.

Supporting Information includes spectroscopic characterization of pristine and defect-induced SWCNTs, including UV–vis–NIR absorption, fluorescence, excitation–emission maps, and Raman analysis. Additional data present fluorescence responses and selectivity tests, real-time spectral evolution upon analyte addition, and complementary FTIR and high-resolution XPS measurements. See DOI: https://doi.org/10.1039/d5nr05162b.

Acknowledgements

G. B. acknowledges the support of the Zuckerman STEM Leadership Program, the ERC NanoNonEq 101039127, the Israel Science Foundation (Grant No. 196/22), the Ministry of Science, Technology, and Space, Israel (Grant No. 1001818370 and 1001944224), the Marian Gertner Institute for Medical Nanosystems at Tel Aviv University, the Zimin Institute for Engineering Solutions Advancing Better Lives, and the Naomi Prawer Kadar Foundation. G. E. acknowledges the scholarship from the Excellency Program of the Faculty of Engineering at Tel Aviv University. The authors thank Dr Bruria Schmerling and Dr Michal Ejgenberg for their help with the Raman measurements.

References

1 N. M. Iverson, G. Bisker, E. Farias, V. Ivanov, J. Ahn, G. N. Wogan and M. S. Strano, Quantitative Tissue Spectroscopy of Near Infrared Fluorescent Nanosensor Implants, *J. Biomed. Nanotechnol.*, 2016, **12**(5), 1035–1047, DOI: 10.1166/jbn.2016.2237.

2 S. Wray, M. Cope, D. T. Delpy, J. S. Wyatt and E. O. R. Reynolds, Characterization of the near Infrared Absorption Spectra of Cytochrome Aa3 and Haemoglobin for the Non-Invasive Monitoring of Cerebral Oxygenation, *Biochim. Biophys. Acta, Bioenerg.*, 1988, **933**(1), 184–192, DOI: 10.1016/0005-2728(88)90069-2.

3 P. W. Barone, R. S. Parker and M. S. Strano, In Vivo Fluorescence Detection of Glucose Using a Single-Walled Carbon Nanotube Optical Sensor: Design, Fluorophore Properties, Advantages, and Disadvantages, *Anal. Chem.*, 2005, **77**(23), 7556–7562, DOI: 10.1021/ac0511997.

4 J. Ackermann, J. T. Metternich, S. Herbertz and S. Kruss, Biosensing with Fluorescent Carbon Nanotubes, *Angew. Chem., Int. Ed.*, 2022, (18), 61, DOI: 10.1002/anie.202112372.

5 E. Hofferber, J. Meier, N. Herrera, J. Stapleton, C. Calkins and N. Iverson, Detection of Single Walled Carbon Nanotube Based Sensors in a Large Mammal, *Nanomedicine*, 2022, **40**, 102489, DOI: 10.1016/j.nano.2021.102489.

6 F. Fan, K. Zeng, Y. Zhu, Y. Zhang, Y. Chen, D. Lv, D. Jia, Y. Chai, X. Chen and Q. Li, Second Near–Infrared Window Fluorescence Materials for In Vivo Dynamic Multiplexed Imaging, *Adv. Funct. Mater.*, 2025, **35**(31), 2422693, DOI: 10.1002/adfm.202422693.

7 R. Acharya, T. V. Patil, S. D. Dutta, J. Lee, K. Ganguly, H. Kim, A. Randhawa and K. Lim, Single–Walled Carbon Nanotube–Based Optical Nano/Biosensors for Biomedical Applications: Role in Bioimaging, Disease Diagnosis, and Biomarkers Detection, *Adv. Mater. Technol.*, 2024, (20), 9, DOI: 10.1002/admt.202400279.

8 Z. Cohen and R. M. Williams, Single-Walled Carbon Nanotubes as Optical Transducers for Nanobiosensors In Vivo, *ACS Nano*, 2024, **18**(52), 35164–35181, DOI: 10.1021/acsnano.4c13076.

9 S. Basu and G. Bisker, Near-Infrared Fluorescent Single-Walled Carbon Nanotubes for Biosensing, *Small*, 2025, **21**(26), 2502542, DOI: 10.1002/SMLL.202502542;JOURNAL:JOURNAL:16136829;PAGEGROUP:STRING:PUBLICATION.

10 C. Farrera, F. Torres Andón and N. Feliu, Carbon Nanotubes as Optical Sensors in Biomedicine, *ACS Nano*, 2017, **11**(11), 10637–10643, DOI: 10.1021/acsnano.7b06701.

11 A. T. Krasley, E. Li, J. M. Galeana, C. Bulumulla, A. G. Beyene and G. S. Demirer, Carbon Nanomaterial Fluorescent Probes and Their Biological Applications, *Chem. Rev.*, 2024, **124**(6), 3085–3185, DOI: 10.1021/acs.chemrev.3c00581.

12 H. Wang and A. A. Boghossian, Covalent Conjugation of Proteins onto Fluorescent Single-Walled Carbon Nanotubes for Biological and Medical Applications, *Mater. Adv.*, 2023, **4**(3), 823–834, DOI: 10.1039/D2MA00714B.

13 M. Yoon, Y. Lee, S. Lee, Y. Cho, D. Koh, S. Shin, C. Tian, Y. Song, J. Kang and S.-Y. Cho, A NIR Fluorescent Single Walled Carbon Nanotube Sensor for Broad-Spectrum Diagnostics, *Sens. Diagn.*, 2024, **3**(2), 203–217, DOI: 10.1039/D3SD00257H.

14 S. S. Shabnum, R. Siranjeevi, C. K. Raj, P. Nivetha and K. Benazir, A Comprehensive Review on Recent Progress in Carbon Nanotubes for Biomedical Application, *Environ. Qual. Manag.*, 2025, **34**(3), e70040, DOI: 10.1002/tqem.70040.

15 A. T. Krasley, S. Chakraborty, L. Vuković and A. G. Beyene, Molecular Determinants of Optical Modulation in SsDNA–Carbon Nanotube Biosensors, *ACS Nano*, 2025, **19**(8), 7804–7820, DOI: 10.1021/acsnano.4c13814.

16 S. Basu, A. Hendler-Neumark and G. Bisker, Dynamic Tracking of Biological Processes Using Near-Infrared Fluorescent Single-Walled Carbon Nanotubes, *ACS Appl. Mater. Interfaces*, 2024, **16**(41), 54960–54975, DOI: 10.1021/acsami.4c10955.

17 S. Nandi, Q. Gresil, B. P. Lambert, F. L. Sebastian, S. Settele, I. Calaresu, J. Estaun-Panzano, A. Lovisotto, C. Mazzocco, B. S. Flavel, E. Bezard, L. Groc, J. Zaumseil and L. Cognet, Ultrashort Carbon Nanotubes with Luminescent Color Centers Are Bright NIR-II Nanoemitters, *ACS Nano*, 2025, **19**(21), 19818–19830, DOI: 10.1021/acsnano.5c02171.

18 N. E. Kallmyer, J. Musielewicz, J. Sutter and N. F. Reuel, Substrate-Wrapped, Single-Walled Carbon Nanotube Probes for Hydrolytic Enzyme Characterization, *Anal. Chem.*, 2018, **90**(8), 5209–5216, DOI: 10.1021/acs.analchem.7b05444.

19 M.-T. Kuo, J. F. Raffaelle, E. M. Waller, V. A. Varaljay, D. Wagner, N. Kelley-Loughnane and N. F. Reuel, Screening Enzymatic Degradation of Polyester Polyurethane with Fluorescent Single-Walled Carbon Nanotube and Polymer Nanoparticle Conjugates, *ACS Nano*, 2023, **17**(17), 17021–17030, DOI: 10.1021/acsnano.3c04347.

20 D. Loewenthal, D. Kamber and G. Bisker, Monitoring the Activity and Inhibition of Cholinesterase Enzymes Using Single-Walled Carbon Nanotube Fluorescent Sensors, *Anal. Chem.*, 2022, **94**(41), 14223–14231, DOI: 10.1021/acs.analchem.2c02471.

21 S. Basu, A. Hendler-Neumark and G. Bisker, Rationally Designed Functionalization of Single–Walled Carbon Nanotubes for Real–Time Monitoring of Cholinesterase Activity and Inhibition in Plasma, *Small*, 2024, **20**(24), 2309481, DOI: 10.1002/smll.202309481.

22 V. Shumeiko, Y. Paltiel, G. Bisker, Z. Hayouka and O. Shoseyov, A Paper-Based Near-Infrared Optical Biosensor for Quantitative Detection of Protease Activity Using Peptide-Encapsulated SWCNTs, *Sensors*, 2020, **20**(18), 5247, DOI: 10.3390/s20185247.

23 Z. Yaari, J. M. Cheung, H. A. Baker, R. S. Frederiksen, P. V. Jena, C. P. Horoszko, F. Jiao, S. Scheuring, M. Luo and D. A. Heller, Nanoreporter of an Enzymatic Suicide Inactivation Pathway, *Nano Lett.*, 2020, **20**(11), 7819–7827, DOI: 10.1021/acs.nanolett.0c01858.

24 S. Basu, A. Hendler-Neumark and G. Bisker, Monitoring Enzyme Activity Using Near-Infrared Fluorescent Single-Walled Carbon Nanotubes, *ACS Sens.*, 2024, **9**(5), 2237–2253, DOI: 10.1021/ACSSENSORS.4C00377/ASSET/IMAGES/LARGE/SE4C00377_0011.JPEG.

25 K. Boonyaves, M. C.-Y. Ang, M. Park, J. Cui, D. T. Khong, G. P. Singh, V. B. Koman, X. Gong, T. K. Porter, S. W. Choi, K. Chung, N.-H. Chua, D. Urano and M. S. Strano, Near-Infrared Fluorescent Carbon Nanotube Sensors for the Plant Hormone Family Gibberellins, *Nano Lett.*, 2023, **23**(3), 916–924, DOI: 10.1021/acs.nanolett.2c04128.

26 R. Ehrlich, A. Hendler-Neumark, V. Wulf, D. Amir and G. Bisker, Optical Nanosensors for Real–Time Feedback on Insulin Secretion by B-Cells, *Small*, 2021, **17**(30), 2101660, DOI: 10.1002/smll.202101660.

27 G. Bisker, N. A. Bakh, M. A. Lee, J. Ahn, M. Park, E. B. O'Connell, N. M. Iverson and M. S. Strano, Insulin Detection Using a Corona Phase Molecular Recognition Site on Single-Walled Carbon Nanotubes, *ACS Sens.*, 2018, **3**(2), 367–377, DOI: 10.1021/acssensors.7b00788.

28 R. M. Williams, C. Lee and D. A. Heller, A Fluorescent Carbon Nanotube Sensor Detects the Metastatic Prostate Cancer Biomarker UPA, *ACS Sens.*, 2018, **3**(9), 1838–1845, DOI: 10.1021/acssensors.8b00631.

29 J. T. Nelson, S. Kim, N. F. Reuel, D. P. Salem, G. Bisker, M. P. Landry, S. Kruss, P. W. Barone, S. Kwak and M. S. Strano, Mechanism of Immobilized Protein A Binding to Immunoglobulin G on Nanosensor Array Surfaces, *Anal. Chem.*, 2015, **87**(16), 8186–8193, DOI: 10.1021/acs.analchem.5b00843.

30 B. C. Satishkumar, L. O. Brown, Y. Gao, C.-C. Wang, H.-L. Wang and S. K. Doorn, Reversible Fluorescence Quenching in Carbon Nanotubes for Biomolecular Sensing, *Nat. Nanotechnol.*, 2007, **2**(9), 560–564, DOI: 10.1038/nnano.2007.261.

31 M. Antman-Passig, Z. Yaari, D. Goerzen, R. Parikh, S. Chatman, L. E. Komer, C. Chen, E. Grabarnik, M. Mathieu, A. Haimovitz-Friedman and D. A. Heller, Nanoreporter Identifies Lysosomal Storage Disease Lipid Accumulation Intracranially, *Nano Lett.*, 2023, **23**(23), 10687–10695, DOI: 10.1021/acs.nanolett.3c02502.

32 F. Ledesma, S. Nishitani, F. J. Cunningham, J. D. Hubbard, D. Yim, A. Lui, L. Chio, A. Murali and M. P. Landry,

Covalent Attachment of Horseradish Peroxidase to Single-Walled Carbon Nanotubes for Hydrogen Peroxide Detection, 2023, vol. 15, DOI: 10.1101/2023.12.14.571773.

33 H. M. Dewey, J. Jones, S. Lucas, S. Hall, N. Sultana, S. M. Abello and J. Budhathoki-Uprety, Carbon Nanotubes for Optical Detection of Quaternary Ammonium Compounds in Complex Media, *ACS Appl. Nano Mater.*, 2023, **6**(17), 15530–15539, DOI: 10.1021/acsanm.3c02219.

34 H. Liu, R. Guo, L. Li, Y. Wen, L. Wang, J. Yan and G. Liu, A NIR Biosensor for the Detection of Silver Ions Based on a Single-Chirality Carbon Nanotube with DNA Wrapping, *ACS Appl. Nano Mater.*, 2025, **8**(27), 13719–13728, DOI: 10.1021/acsanm.5c01869.

35 J. Mun, N. Navarro, S. Jeong, N. Ouassil, E. Leem, A. G. Beyene and M. P. Landry, Near-Infrared Nanosensors Enable Optical Imaging of Oxytocin with Selectivity over Vasopressin in Acute Mouse Brain Slices, *Proc. Natl. Acad. Sci. U. S. A.*, 2024, **121**(26), e2314795121, DOI: 10.1073/pnas.2314795121.

36 M. M. Safaee, M. Gravely and D. Roxbury, A Wearable Optical Microfibrous Biomaterial with Encapsulated Nanosensors Enables Wireless Monitoring of Oxidative Stress, *Adv. Funct. Mater.*, 2021, **31**(13), 2006254, DOI: 10.1002/adfm.202006254.

37 D. T. Khong, K. V. Vu, B. J. R. Sng, I. K. Y. Choi, T. K. Porter, J. Cui, X. Gong, S. Wang, N. H. Nguyen, M. C.-Y. Ang, M. Park, T. T. S. Lew, S. I. Loh, R. Ahsim, H. J. Chin, G. P. Singh, M. B. Chan-Park, N.-H. Chua, M. S. Strano and I.-C. Jang, A Near-Infrared Fluorescent Nanosensor for Direct and Real-Time Measurement of Indole-3-Acetic Acid in Plants, *ACS Nano*, 2025, **19**(16), 15302–15321, DOI: 10.1021/acsnano.4c13556.

38 J. Chen, Y. Li, J. Wu, J. Liu, X. Zhou, Z. Li, K. Tang, L. Shi, Z. Zhang and Z. Lin, Ordered DNA-Wrapped Single-Chirality Carbon Nanotubes Enable an Unparalleled Sensing Platform for Copper Ion Detection, *ACS Nano*, 2025, **19**(31), 28743–28754, DOI: 10.1021/acsnano.5c08364.

39 N. K. Subbaiyan, S. Cambré, A. N. G. Parra-Vasquez, E. H. Hároz, S. K. Doorn and J. G. Duque, Role of Surfactants and Salt in Aqueous Two-Phase Separation of Carbon Nanotubes toward Simple Chirality Isolation, *ACS Nano*, 2014, **8**(2), 1619–1628, DOI: 10.1021/nn405934y.

40 J. A. Fagan, Aqueous Two-Polymer Phase Extraction of Single-Wall Carbon Nanotubes Using Surfactants, *Nanoscale Adv.*, 2019, **1**(9), 3307–3324, DOI: 10.1039/C9NA00280D.

41 D. Just, A. Dzienia, K. Z. Milowska, A. Mielańczyk and D. Janas, High-Yield and Chirality-Selective Isolation of Single-Walled Carbon Nanotubes Using Conjugated Polymers and Small Molecular Chaperones, *Mater. Horiz.*, 2024, **11**(3), 758–767, DOI: 10.1039/D3MH01687K.

42 Y. Lee, W. Kim, Y. Cho, M. Yoon, S. Lee, J. Lee, S. Oh, Y. Song, B. J. Lee, Y. Kim and S.-Y. Cho, Rational Design of 3D Polymer Corona Interfaces of Single-Walled Carbon Nanotubes for Receptor-Free Virus Recognition, *ACS Nano*, 2024, **18**(20), 13214–13225, DOI: 10.1021/acsnano.4c02130.

43 D. Fong and A. Adronov, Recent Developments in the Selective Dispersion of Single-Walled Carbon Nanotubes Using Conjugated Polymers, *Chem. Sci.*, 2017, **8**(11), 7292–7305, DOI: 10.1039/C7SC02942J.

44 J. M. Salazar-Rios, W. Talsma, V. Derenskyi, W. Gomulya, T. Keller, M. Fritsch, S. Kowalski, E. Preis, M. Wang, S. Allard, G. C. Bazan, U. Scherf, M. C. dos Santos and M. A. Loi, Understanding the Selection Mechanism of the Polymer Wrapping Technique toward Semiconducting Carbon Nanotubes, *Small Methods*, 2018, **2**(4), 1700335, DOI: 10.1002/smtd.201700335.

45 A. Hendler-Neumark and G. Bisker, Fluorescent Single-Walled Carbon Nanotubes for Protein Detection, *Sensors*, 2019, **19**(24), 5403, DOI: 10.3390/s19245403.

46 R. L. Pinals, D. Yang, A. Lui, W. Cao and M. P. Landry, Corona Exchange Dynamics on Carbon Nanotubes by Multiplexed Fluorescence Monitoring, *J. Am. Chem. Soc.*, 2020, **142**(3), 1254–1264, DOI: 10.1021/jacs.9b09617.

47 V. Wulf and G. Bisker, Integrating Single-Walled Carbon Nanotubes into Supramolecular Assemblies: From Basic Interactions to Emerging Applications, *ACS Nano*, 2024, **18**(43), 29380–29393, DOI: 10.1021/acsnano.4c06843.

48 M. Park, D. P. Salem, D. Parviz, X. Gong, K. S. Silmore, T. T. S. Lew, D. T. Khong, M. C.-Y. Ang, S.-Y. Kwak, M. B. Chan-Park and M. S. Strano, Measuring the Accessible Surface Area within the Nanoparticle Corona Using Molecular Probe Adsorption, *Nano Lett.*, 2019, **19**(11), 7712–7724, DOI: 10.1021/acs.nanolett.9b02647.

49 S. Lee, G. Ryu, S. Shin, W. Kim, M. Yoon, Y. Kim, S. Park, Y. Kim and S.-Y. Cho, Clinically-Driven Rapidly Developed Nanoparticle Corona for Label-Free Cerebrospinal Fluid Leakage Detection, *ACS Nano*, 2025, **19**(1), 950–962, DOI: 10.1021/acsnano.4c12364.

50 S. Kruss, M. P. Landry, E. Vander Ende, B. M. A. Lima, N. F. Reuel, J. Zhang, J. Nelson, B. Mu, A. Hilmer and M. Strano, Neurotransmitter Detection Using Corona Phase Molecular Recognition on Fluorescent Single-Walled Carbon Nanotube Sensors, *J. Am. Chem. Soc.*, 2014, **136**(2), 713–724, DOI: 10.1021/ja410433b.

51 N. Sultana, H. M. Dewey, A. G. Arellano and J. Budhathoki-Uprety, Understanding the Molecular Assemblies of Single Walled Carbon Nanotubes and Tailoring Their Photoluminescence for the Next-Generation Optical Nanosensors, *Chem. Mater.*, 2024, **36**(9), 4034–4053, DOI: 10.1021/acs.chemmater.4c00232.

52 G. Bisker, J. Dong, H. D. Park, N. M. Iverson, J. Ahn, J. T. Nelson, M. P. Landry, S. Kruss and M. S. Strano, Protein-Targeted Corona Phase Molecular Recognition, *Nat. Commun.*, 2016, **7**(1), 10241, DOI: 10.1038/ncomms10241.

53 C.-W. Lin, S. M. Bachilo, Y. Zheng, U. Tsedev, S. Huang, R. B. Weisman and A. M. Belcher, Creating Fluorescent Quantum Defects in Carbon Nanotubes Using Hypochlorite and Light, *Nat. Commun.*, 2019, **10**(1), 2874, DOI: 10.1038/s41467-019-10917-3.

54 S. Settele, F. Stammer, F. L. Sebastian, S. Lindenthal, S. R. Wald, H. Li, B. S. Flavel and J. Zaumseil, Easy Access

to Bright Oxygen Defects in Biocompatible Single-Walled Carbon Nanotubes via a Fenton-like Reaction, *ACS Nano*, 2024, **18**(31), 20667–20678, DOI: 10.1021/acsnano.4c06448.

55 S. Basu, The Importance of Defects in Controlling the Chemistry of Single-Walled Carbon Nanotubes, *J. Phys. Chem. Lett.*, 2025, **22**, 5128–5139, DOI: 10.1021/acs.jpclett.5c00811.

56 Y. Niidome, R. Wakabayashi, M. Goto, T. Fujigaya and T. Shiraki, Protein-Structure-Dependent Spectral Shifts of near-Infrared Photoluminescence from Locally Functionalized Single-Walled Carbon Nanotubes Based on Avidin–Biotin Interactions, *Nanoscale*, 2022, **14**(36), 13090–13097, DOI: 10.1039/D2NR01440H.

57 K. Hayashi, Y. Niidome, T. Shiga, B. Yu, Y. Nakagawa, D. Janas, T. Fujigaya and T. Shiraki, Azide Modification Forming Luminescent Sp ^{2} Defects on Single-Walled Carbon Nanotubes for near-Infrared Defect Photoluminescence, *Chem. Commun.*, 2022, **58**(81), 11422–11425, DOI: 10.1039/D2CC04492G.

58 S. Basu, D. Just, A. Hendler-Neumark, D. Janas and G. Bisker, Post-Functionalization Modification as a Modular Strategy for Size-Selective Fluorescence Response of Single-Walled Carbon Nanotubes to Polycyclic Aromatic Hydrocarbons, *Mater. Horiz.*, 2026, **13**(5), 2520–2536, DOI: 10.1039/D5MH02318A.

59 A. H. Brozena, M. Kim, L. R. Powell and Y. Wang, Controlling the Optical Properties of Carbon Nanotubes with Organic Colour-Centre Quantum Defects, *Nat. Rev. Chem.*, 2019, **3**(6), 375–392, DOI: 10.1038/s41570-019-0103-5.

60 A. K. Mandal, X. Wu, J. S. Ferreira, M. Kim, L. R. Powell, H. Kwon, L. Groc, Y. Wang and L. Cognet, Fluorescent Sp3 Defect-Tailored Carbon Nanotubes Enable NIR-II Single Particle Imaging in Live Brain Slices at Ultra-Low Excitation Doses, *Sci. Rep.*, 2020, **10**(1), 5286, DOI: 10.1038/s41598-020-62201-w.

61 B. J. Heppe, N. Dzombic, J. M. Keil, X.-L. Sun and G. Ao, Solvent Isotope Effects on the Creation of Fluorescent Quantum Defects in Carbon Nanotubes by Aryl Diazonium Chemistry, *J. Am. Chem. Soc.*, 2023, **145**(47), 25621–25631, DOI: 10.1021/jacs.3c07341.

62 S. Settele, C. A. Schrage, S. Jung, E. Michel, H. Li, B. S. Flavel, A. S. K. Hashmi, S. Kruss and J. Zaumseil, Ratiometric Fluorescent Sensing of Pyrophosphate with Sp ^{3}-Functionalized Single-Walled Carbon Nanotubes, *Nat. Commun.*, 2024, **15**(1), 706, DOI: 10.1038/s41467-024-45052-1.

63 Y. Niidome, H. Matsumoto, R. Hamano, K. Kato, T. Fujigaya and T. Shiraki, Polymer Wrapping State Changes at Defect Sites of Locally Functionalized Single-Walled Carbon Nanotubes, *J. Phys. Chem. C*, 2024, **128**(12), 5146–5155, DOI: 10.1021/acs.jpcc.3c07692.

64 V. B. Espinoza, S. M. Bachilo, Y. Zheng, H. Htoon and R. B. Weisman, Complexity in the Photofunctionalization of Single-Wall Carbon Nanotubes with Hypochlorite, *ACS Nano*, 2025, **19**(2), 2497–2506, DOI: 10.1021/acsnano.4c13605.

65 S. Basu, A. Hendler-Neumark and G. Bisker, Ratiometric Normalization of Near-Infrared Fluorescence in Defect-Engineered Single-Walled Carbon Nanotubes for Cholesterol Detection, *J. Phys. Chem. Lett.*, 2024, 10425–10434, DOI: 10.1021/ACS.JPCLETT.4C02022/ASSET/IMAGES/LARGE/JZ4C02022_0004.JPEG.

66 E. E. Christensen, M. Amin, T. M. Tumiel and T. D. Krauss, Localized Charge on Surfactant-Wrapped Single-Walled Carbon Nanotubes, *J. Phys. Chem. Lett.*, 2022, **13**(46), 10705–10712, DOI: 10.1021/acs.jpclett.2c02650.

67 J. Zhang, M. P. Landry, P. W. Barone, J. H. Kim, S. Lin, Z. W. Ulissi, D. Lin, B. Mu, A. A. Boghossian, A. J. Hilmer, A. Rwei, A. C. Hinckley, S. Kruss, M. A. Shandell, N. Nair, S. Blake, F. Şen, S. Şen, R. G. Croy, D. Li, K. Yum, J. H. Ahn, H. Jin, D. A. Heller, J. M. Essigmann, D. Blankschtein and M. S. Strano, Molecular Recognition Using Corona Phase Complexes Made of Synthetic Polymers Adsorbed on Carbon Nanotubes, *Nat. Nanotechnol.*, 2013, **8**(12), 959–968, DOI: 10.1038/NNANO.2013.236;SUBJMETA=350,59,61,631,639,925;KWRD=BIOSENSORS.

68 S. Basu, A. Hendler-Neumark and G. Bisker, Role of Oxygen Defects in Eliciting a Divergent Fluorescence Response of Single-Walled Carbon Nanotubes to Dopamine and Serotonin, *ACS Nano*, 2024, **18**(50), 34134–34146, DOI: 10.1021/acsnano.4c10360.

69 A. J. Gillen, D. J. Siefman, S. J. Wu, C. Bourmaud, B. Lambert and A. A. Boghossian, Templating Colloidal Sieves for Tuning Nanotube Surface Interactions and Optical Sensor Responses, *J. Colloid Interface Sci.*, 2020, **565**, 55–62, DOI: 10.1016/J.JCIS.2019.12.058.

70 A. K. Greaves and R. J. Letcher, A Review of Organophosphate Esters in the Environment from Biological Effects to Distribution and Fate, *Bull. Environ. Contam. Toxicol.*, 2017, **98**(1), 2–7, DOI: 10.1007/s00128-016-1898-0.

71 B. N. Okolonkwo, C. F. Amadi and O. E. Chimekagbe, Organophosphates Toxicity: Pathophysiology, Diagnosis, and Treatment, *Asian J. Biochem. Genet. Mol. Biol.*, 2022, 27–37, DOI: 10.9734/ajbgmb/2022/v12i230290.

72 V. G. V. Dutt, S. Akhil and N. Mishra, Surface Passivation Strategies for Improving Photoluminescence and Stability of Cesium Lead Halide Perovskite Nanocrystals, *ChemNanoMat*, 2020, **6**(12), 1730–1742, DOI: 10.1002/cnma.202000495.

73 X. Li, S. Zhang, S. A. Kulinich, Y. Liu and H. Zeng, Engineering Surface States of Carbon Dots to Achieve Controllable Luminescence for Solid-Luminescent Composites and Sensitive Be2+ Detection, *Sci. Rep.*, 2014, **4**(1), 4976, DOI: 10.1038/srep04976.

74 W. Dong, W. Qiao, S. Xiong, J. Yang, X. Wang, L. Ding, Y. Yao and Q. Bao, Surface Passivation and Energetic Modification Suppress Nonradiative Recombination in Perovskite Solar Cells, *Nanomicro Lett.*, 2022, **14**(1), 108, DOI: 10.1007/s40820-022-00854-0.

75 L. Xu, J. Li, B. Cai, J. Song, F. Zhang, T. Fang and H. Zeng, A Bilateral Interfacial Passivation Strategy Promoting Efficiency and Stability of Perovskite Quantum Dot Light-Emitting Diodes, *Nat. Commun.*, 2020, **11**(1), 3902, DOI: 10.1038/s41467-020-17633-3.

76 S. L. Chen, W. M. Chen, F. Ishikawa and I. A. Buyanova, Suppression of Non-Radiative Surface Recombination by N Incorporation in GaAs/GaNAs Core/Shell Nanowires, *Sci. Rep.*, 2015, **5**(1), 11653, DOI: 10.1038/srep11653.

77 J. S. Pappalardo, J.-R. Macairan, A. Macina, A. Poulhazan, V. Quattrocchi, I. Marcotte and R. Naccache, Effects of Polydopamine-Passivation on the Optical Properties of Carbon Dots and Its Potential Use *in Vivo*, *Phys. Chem. Chem. Phys.*, 2020, **22**(29), 16595–16605, DOI: 10.1039/D0CP01938K.

78 J. Zaumseil, Luminescent Defects in Single–Walled Carbon Nanotubes for Applications, *Adv. Opt. Mater.*, 2022, **10**(2), 2101576, DOI: 10.1002/adom.202101576.

79 K. Y. Foo and B. H. Hameed, Insights into the Modeling of Adsorption Isotherm Systems, *Chem. Eng. J.*, 2010, **156**(1), 2–10, DOI: 10.1016/j.cej.2009.09.013.

80 S. Oldemeyer, M. La Greca, P. Langner, K.-L. Lê Công, R. Schlesinger and J. Heberle, Nanosecond Transient IR Spectroscopy of Halorhodopsin in Living Cells, *J. Am. Chem. Soc.*, 2024, **146**(28), 19118–19127, DOI: 10.1021/jacs.4c03891.

81 V. V. Butova, V. R. Zdravkova, O. A. Burachevskaia, A. A. Tereshchenko, P. S. Shestakova and K. I. Hadjiivanov, In Situ FTIR Spectroscopy for Scanning Accessible Active Sites in Defect-Engineered UiO-66, *Nanomaterials*, 2023, **13**(10), 1675, DOI: 10.3390/nano13101675.

82 A. Dawes, N. J. Mason and H. J. Fraser, Using the C–O Stretch to Unravel the Nature of Hydrogen Bonding in Low-Temperature Solid Methanol–Water Condensates, *Phys. Chem. Chem. Phys.*, 2016, **18**(2), 1245–1257, DOI: 10.1039/C5CP05299H.

83 T. Duguet, C. Bessaguet, M. Aufray, J. Esvan, C. Charvillat, C. Vahlas and C. Lacaze-Dufaure, Toward a Computational and Experimental Model of a Poly-Epoxy Surface, *Appl. Surf. Sci.*, 2015, **324**, 605–611, DOI: 10.1016/j.apsusc.2014.10.096.

84 A. S. Singh, J. H. Advani and A. V. Biradar, Phosphonate Functionalized Carbon Spheres as Brønsted Acid Catalysts for the Valorization of Bio-Renewable α-Pinene Oxide to *Trans* -Carveol, *Dalton Trans.*, 2020, **49**(21), 7210–7217, DOI: 10.1039/D0DT00921K.

85 D. Li, M. Sumiya, S. Fuke, D. Yang, D. Que, Y. Suzuki and Y. Fukuda, Selective Etching of GaN Polar Surface in Potassium Hydroxide Solution Studied by X-Ray Photoelectron Spectroscopy, *J. Appl. Phys.*, 2001, **90**(8), 4219–4223, DOI: 10.1063/1.1402966.

86 K. Zhang, Z. Zhuo, G. Fan, Z. Wang, S. Chen, L. Xu, Y. Wen and P. Wang, Nano-ZnS Decorated Hierarchically Porous Carbon Electrocatalyst with Multiple Enzyme-like Activities as a Nanozyme Sensing Platform for Simultaneous Detection of Dopamine, Uric Acid, Guanine, and Adenine, *Nanoscale*, 2021, **13**(47), 20078–20090, DOI: 10.1039/D1NR06017A.

87 G. D. Khattak, M. A. Salim, L. E. Wenger and A. H. Gilani, X-Ray, Photoelectron Spectroscopy (XPS) and Magnetic Susceptibility Studies of Copper–Vanadium Phosphate Glasses, *J. Non-Cryst. Solids*, 2000, **262**(1–3), 66–79, DOI: 10.1016/S0022-3093(99)00700-0.

88 O. K. Kari, J. Ndika, P. Parkkila, A. Louna, T. Lajunen, A. Puustinen, T. Viitala, H. Alenius and A. Urtti, *In Situ* Analysis of Liposome Hard and Soft Protein Corona Structure and Composition in a Single Label-Free Workflow, *Nanoscale*, 2020, **12**(3), 1728–1741, DOI: 10.1039/C9NR08186K.

89 H. M. Dewey, A. Lamb and J. Budhathoki-Uprety, Recent Advances on Applications of Single-Walled Carbon Nanotubes as Cutting-Edge Optical Nanosensors for Biosensing Technologies, *Nanoscale*, 2024, **16**(35), 16344–16375, DOI: 10.1039/D4NR01892C.

90 S. Piletsky, E. Keblish, A. Goffin, X. Jin, M. Zheng, M. Kim and D. Heller, *Handle-Free Conjugation of Small Molecules Generates Tunable Emissive Defects on Carbon Nanotubes*, 2025, vol. 15, DOI: 10.26434/chemrxiv-2025-5dxsd.